Entanglement, anomalies, and Mathisson's helices

Piermarco Fonda,[1,*] Diego Liska,[2,†] and Álvaro Véliz-Osorio[3,‡]

[1]*Instituut-Lorentz, Universiteit Leiden, P.O. Box 9506, 2300 RA Leiden, The Netherlands*
[2]*Department of Physics, Universidad del Valle de Guatemala, 18 Avenida 11-95, Zona 15 Guatemala, Guatemala*
[3]*M. Smoluchowski Institute of Physics, Jagiellonian University, Łojasiewicza 11, 30-348 Kraków, Poland*

(Received 4 September 2018; published 14 February 2019)

We study the physical properties of a length-torsion functional which encodes the holographic entanglement entropy for $(1+1)$-dimensional theories with chiral anomalies. Previously, we have shown that its extremal curves correspond to the mysterious Mathisson's helical motions for the centroids of spinning bodies. We explore the properties of these helices in domain-wall backgrounds using both analytic and numerical techniques. Using these insights we derive an entropic c-function $c_{\mathrm{Hel}}(\ell)$ which can be succinctly expressed in terms of Noether charges conserved along these helical motions. While for generic values of the anomaly there is some ambiguity in the definition of $c_{\mathrm{Hel}}(\ell)$, we argue that at the chiral point this ambiguity is absent.

DOI: 10.1103/PhysRevD.99.046007

I. INTRODUCTION AND SUMMARY

Zamolodchikov's c-theorem [1] provides a deep insight into the general properties of quantum field theories. It states that for every Poincaré invariant local theory in two dimensions there exists a function of the couplings that decreases monotonically along renormalization group (RG) flows. Furthermore, if the theory in question is conformal, this function is constant and matches the central charge of the conformal field theory (CFT). This theorem formalizes the intuition that information regarding the microscopic details of the theory is lost as one studies it macroscopically, meaning that RG flows are irreversible. It is possible to generalize this result to chiral theories [2]: in this case, two distinct c-functions can be defined, one for left movers and one for right movers. As demonstrated in [2], the difference of these functions is constant along RG flows. This difference quantifies the number of degrees of freedom that are precluded from becoming massive at large distances. The fact that this quantity remains constant along the flow is a two-dimensional version of 't Hooft's anomaly matching condition for the chiral anomaly. In contrast, the sum of these functions decreases monotonically along the RG just as the nonchiral c-function.

*fonda@lorentz.leidenuniv.nl
†lis14392@uvg.edu.gt
‡aveliz@gmail.com

It is well known that there is an intimate relationship between gravity in AdS_3 and two-dimensional CFTs. Indeed, as discovered by Brown and Henneaux [3], the asymptotic symmetry algebra for Einstein gravity in AdS_3 corresponds to a left- and a right-moving Virasoro algebra with identical central charges. In this work, we are interested in theories with chiral anomalies for which there is a mismatch between left- and right-moving central charges. On the gravity side, this is implemented by regarding AdS_3 as a solution of topologically massive gravity (TMG) [4]. In which case, the difference between the central charges is proportional to the Compton wavelength of the massive graviton [5]. It has been argued that for arbitrary values of the graviton's mass, TMG violates either unitarity or positivity [6]. However, at the critical point where the graviton's Compton wavelength matches the AdS_3 radius these problems are absent. At this point, the dual central charges read

$$(c_L, c_R) = (0, 3L/G_3), \tag{1.1}$$

where L is the AdS_3 radius and G_3 is the three-dimensional Newton's constant. Condition (1.1) is known as the chiral point, and the theory associated with it, called chiral gravity, has Bañados-Teitelboim-Zanelli black holes and gravitons with non-negative mass [6].

The physics of RG flows can be probed using quantum information theoretic quantities such as entanglement entropy (EE). For $(1+1)$-dimensional quantum field theories, it is well known that the EE of a spacelike interval of length ℓ exhibits logarithmic divergences. Nonetheless,

it is possible to extract its universal part by computing the *renormalized entanglement entropy* (REE) [7,8]

$$\hat{S}_{EE}(\ell) = \ell \frac{d}{d\ell} S_{EE}(\ell). \tag{1.2}$$

If the field theory in question is conformal, then the REE is proportional to the central charge and for a RG flow interpolating between two CFTs it was shown by Casini and Huerta [7] that (1.2) interpolates monotonically between their respective central charges, a result which furnishes an *entropic* proof of Zamolodchikov's c-theorem. This story has a gravitational counterpart: it was shown by Ryu and Takayanagi (RT) [9] that calculating EE for field theories with a dual gravitational description involves finding a suitable extremal surface in an asymptotically anti–de Sitter (AdS) spacetime. Whenever the dual gravitational description corresponds to Einstein gravity, the relevant surface extremizes the area functional with properly chosen boundary conditions. In the case of $(1+1)$-dimensional theories, the EE of a spacelike interval of length ℓ is obtained through a bulk curve $\gamma(\ell)$ which extremizes the functional

$$\mathcal{F}_0[\gamma] = \mathfrak{m}\mathrm{L}[\gamma], \tag{1.3}$$

whose end points correspond to those of the boundary interval. The entanglement entropy associated with the interval is given by the length of this curve, i.e.,

$$S_{\mathrm{EE}}(\ell) = \mathcal{F}_0[\gamma(\ell)], \tag{1.4}$$

for the appropriate value of $\mathfrak{m}$. Using the gravitational duals of RG flows it is possible to construct an entropic c-function out of geodesic lengths [10].

It is often the case that the dual gravitational description of a field theory does not correspond to Einstein gravity. In such cases, the holographic entanglement entropy (HEE) can still be computed by geometrical means but important modifications to the RT prescription are required [11,12]. The functional to be extremized in order to calculate the HEE can be deduced from the dual gravitational theory via the replica trick. The equations resulting from extremizing these functionals are, in general, of higher order than the geodesic equations. This raises the question of which extra conditions must be provided to determine the extremum that correctly computes the HEE. For AdS backgrounds one can simply resort to matching the result expected from the dual CFT [13]. However, as far as we are aware, this question remains open for more general metrics, such as those encoding RG flows. As we shall see, although the correct extrema cannot be singled out in general, it is possible to establish some necessary conditions to restrict the space of admissible extrema.

As mentioned above, $(1+1)$-dimensional conformal field theories with chiral anomalies require a modification of the bulk theory, and hence the RT prescription must be modified accordingly. The authors of [14] have shown that, in this context, the holographic entanglement entropy is encoded by the functional

$$\mathcal{F}[\gamma] = \mathfrak{m}\mathrm{L}[\gamma] + \mathfrak{s}\int_\gamma \tau, \tag{1.5}$$

where τ is the extrinsic torsion of the curve γ, while $\mathfrak{m}$ and $\mathfrak{s}$ are suitably chosen constants. In the following, we would like to proceed in an analogous fashion to [10]. First, we consider a boundary interval of proper length ℓ and join its end points $(X_\pm, T_\pm)$ with an extremum of (1.5). Then we must elucidate how the on-shell value of (1.5) changes with ℓ in order to find the analogue of Eq. (1.2). Difficulties arise from the fact that the extrema of (1.5) correspond to Mathisson's helical motions of spinning bodies [15] which are, in general, more complicated than geodesics. Moreover, since Mathisson's helices are solutions to higher order equations, it is necessary to fix more boundary conditions in order to single out a solution. Nevertheless, these adversities can be surmounted and in the present work we show that this geometrical problem has a succinct solution. We find that the renormalized $\mathcal{F}[\gamma]$ is given by

$$\hat{\mathcal{F}} \equiv \ell \frac{d\mathcal{F}}{d\ell} = (T_+ - T_-)\mathcal{Q}_t + (X_+ - X_-)\mathcal{Q}_x, \tag{1.6}$$

where $\mathcal{Q}_t$ and $\mathcal{Q}_x$ are conserved charges associated with rigid translations of relativistic spinning bodies.

Equation (1.6) is valid for any continuously varying family of Mathisson's helices connecting the interval's end points as we change ℓ. In general, there exist an infinite number of such families. This is a consequence of the aforementioned ambiguity in choosing the correct extrema to compute the HEE. However, if we are to regard Eq. (1.6) as a *bona fide* probe for entanglement entropy, then it must at least obey the strong subadditivity property, which implies that (1.6) must decrease monotonically with ℓ. By imposing this requirement we can restrict the space of allowed solutions. As we shall see, as one approaches the chiral point, this restriction becomes stringent enough to single out a unique family of helices with which we can associate the quantity

$$\frac{c_{\mathrm{Hel}}(\ell)}{3} \equiv \hat{\mathcal{F}}(\ell) = \frac{\mathcal{Q}_x}{\mathcal{Q}_t}. \tag{1.7}$$

This function displays the features expected by an entropic c-function for a wide variety of examples; namely, in a renormalization group flow setting, it monotonically interpolates between two CFT central charges.

II. SHAPE EQUATIONS AND ANOMALIES

In this section we study the general properties of extremal curves associated with the functional (1.5).

The following discussion requires some acquaintance with extrinsic geometric terminology, and we refer the reader to [13,15] for a detailed discussion and notation. To describe the geometry of a curve embedded in a three-manifold we must introduce a *moving frame* composed of a normalized tangent vector t^μ and two normal vectors n^μ_A, with $A = 1, 2$, defined by

$$t_\mu n^\mu_A = 0, \qquad g_{\mu\nu} n^\mu_A n^\nu_B = \eta_{AB}, \tag{2.1}$$

where $\eta_{AB} = \mathrm{diag}(1, -1)$. Using this moving frame we define the extrinsic curvatures and torsion:

$$k^A = t^\mu \mathcal{D}_s n^A_\mu, \qquad \tau = \frac{1}{2}\epsilon_{AB}(n^A_\mu \mathcal{D}_s n^{B\mu}), \tag{2.2}$$

where $\mathcal{D}_s = t^\mu \nabla_\mu$ is the directional derivative along the curve. In terms of these quantities, the equations that dictate the shape of the extremal curves can be written as [15]

$$\mathfrak{m} k_A + \mathfrak{s}\epsilon_{AB}[(\tilde{D}k)^B + R_s{}^B] = 0, \tag{2.3}$$

where

$$(\tilde{D}V)^A = \partial_s V^A + \tau \epsilon^{AB}\eta_{BC} V^C \tag{2.4}$$

and

$$R_s{}^B = t^\mu n^{\nu B} R_{\mu\nu}. \tag{2.5}$$

Using Frenet-Serret extrinsic quantities, which are those associated with a moving frame where the extrinsic curvature in one of the normal directions is set to vanish identically, the shape equations take the convenient form

$$\begin{aligned} \partial_s k^2_{\mathrm{FS}} &= -2R_s{}^B k_B, \\ k^2_{\mathrm{FS}}(\mathfrak{m} - \mathfrak{s}\tau_{\mathrm{FS}}) &= -\mathfrak{s}\epsilon_{AB} k^A R_s{}^B, \end{aligned} \tag{2.6}$$

where $k^2_{\mathrm{FS}} = \eta_{AB} k^A k^B$ is the total curvature and τ_{FS} is the torsion in the Frenet-Serret frame. From these equations it clearly follows that in a maximally symmetric ambient space, the total curvature is constant along extremal curves. Moreover, provided $k^2_{\mathrm{FS}} \neq 0$, the Frenet-Serret torsion reads

$$\tau_{\mathrm{FS}} = \frac{\mathfrak{m}}{\mathfrak{s}}, \tag{2.7}$$

and it is thus fixed by the couplings of the theory.

It is important to point out that the *shape equations* (2.3) are closely related to the Mathisson-Papapetrou-Dixon (MPD) equations [16–18]

$$\mathcal{D}_s p^\lambda = -\frac{1}{2} t^\nu \mathcal{S}^{\rho\sigma} R^\lambda{}_{\nu\rho\sigma}, \tag{2.8}$$

$$\mathcal{D}_s \mathcal{S}^{\mu\nu} = p^\mu t^\nu - t^\mu p^\nu, \tag{2.9}$$

for the momentum p^μ and spin $\mathcal{S}^{\mu\nu}$ of an extended body in the pole-dipole approximation. The equivalence between the two systems holds only when the above are supplemented with the Mathisson-Pirani (MP) condition [19,20]

$$\mathcal{S}^{\mu\nu} t_\mu = 0, \tag{2.10}$$

upon identifying

$$-p^\mu = \mathfrak{m} t^\mu + \mathfrak{s}\epsilon_{AB} k^A n^{B\mu}, \qquad \mathcal{S}^{\mu\nu} = \mathfrak{s}\epsilon_{AB} n^{A\mu} n^{B\nu}. \tag{2.11}$$

Solutions $\gamma(s)$ to the system MPD with MP conditions are known in the literature as *Mathisson's helices* [21]; hereafter we use this nomenclature for the extrema of (1.5). Regarding the solutions to the shape equations (2.3) as the trajectories of spinning bodies naturally evokes concepts from dynamics. For instance, the idea that symmetries of the ambient manifold induce conserved quantities along trajectories inexorably comes to mind. Concretely, with any Killing field ξ_μ in the ambient manifold we can associate a *charge*

$$\mathcal{Q}_\xi[\gamma] = \xi_\mu p^\mu + \frac{1}{2}\mathcal{S}^{\mu\nu}\nabla_\mu \xi_\nu, \tag{2.12}$$

which is conserved along Mathisson helices [22]. These charges will prove crucial in the arguments we develop in the forthcoming sections. It is straightforward to verify that (2.12) is conserved using the MPD equations. Nevertheless, we provide a derivation of these charges using Noether's theorem in Appendix B.

A. AdS_3 helices

The shape equations (2.3) can be solved analytically for maximally symmetric ambient manifolds. In [15] all possible solutions in AdS_3 spacetime,

$$ds^2 = \frac{L^2}{z^2}(\eta_{ab} dx^a dx^b + dz^2), \tag{2.13}$$

were classified in terms of their Frenet-Serret curvature k^2_{FS} and torsion τ_{FS}. Moreover, since the Frenet-Serret torsion is fixed uniquely by the couplings of the theory ($\tau_{\mathrm{FS}} = \mathfrak{m}/\mathfrak{s}$), the only free parameter is the curvature k^2_{FS}. For the purposes of the present discussion, we are concerned with solutions which connect spacelike separated points in the boundary. This requirement imposes restrictions on the allowed values of k^2_{FS} relative to τ_{FS} and the AdS_3 radius, either

$$0 \leq k^2_{\mathrm{FS}} \leq \left(\frac{1}{L} - \tau_{\mathrm{FS}}\right)^2 \quad \text{or} \quad k^2_{\mathrm{FS}} \leq 0. \tag{2.14}$$

In the first case $|L\tau_{\mathrm{FS}}| < 1$ and the solution must be isometric[1] to

$$\gamma^{\mu}_{I_a} = \frac{L}{a\cosh\lambda_- s + b\cosh\lambda_+ s}\begin{pmatrix} a\sinh\lambda_- s \\ b\sinh\lambda_+ s \\ L \end{pmatrix}, \quad (2.15)$$

where $a^2 + L^2 = b^2$ and $a^2\lambda_-^2 + 1 = b^2\lambda_+^2$. In the latter instance, solutions are isometric to

$$\gamma^{\mu}_{I_c} = \frac{L}{a\sinh\lambda_- s + b\cosh\lambda_+ s}\begin{pmatrix} a\cosh\lambda_- s \\ b\sinh\lambda_+ s \\ L \end{pmatrix}, \quad (2.16)$$

with $a^2 + b^2 = L^2$ and $a^2\lambda_-^2 + b^2\lambda_+^2 = 1$. In both cases we have

$$\lambda_\pm = \sqrt{\frac{1}{2}\left(-\Lambda \pm \sqrt{\Lambda^2 - 4\frac{\tau_{\mathrm{FS}}^2}{L^2}}\right)}, \quad (2.17)$$

where

$$\Lambda = k_{\mathrm{FS}}^2 - \frac{1}{L^2} - \tau_{\mathrm{FS}}^2. \quad (2.18)$$

Clearly, two spacelike separated points on the boundary can be joined via a bulk geodesic isometric to

$$\gamma^{\mu}_{\mathrm{Geo}} = \begin{pmatrix} 0 \\ L\tanh(s/L) \\ L\,\mathrm{sech}(s/L) \end{pmatrix}, \quad (2.19)$$

which can be retrieved from either Eq. (2.15) or Eq. (2.16) by setting $\lambda_+ = 1/L$. The curves (2.15), (2.16), and (2.19) all end on boundary intervals of length $\ell = 2L$, and every other boundary length can be obtained by a rescaling.

Once the extremal curves have been constructed, we must proceed to evaluate the functional (1.5) on these solutions. What makes this functional able to capture the physics of gravitational anomalies is that in contrast to the curve's length, the torsion term is not invariant under boosts [14]. Observe that the normal vectors in the moving frame (2.1) are defined up to local boosts: the change $n^{A\mu} \to \tilde{n}^{A\mu} = \lambda^A{}_B[\psi(s)]n^{B\mu}$, with

$$\lambda^A{}_B[\psi(s)] = \begin{pmatrix} \cosh(\psi(s)) & \sinh(\psi(s)) \\ \sinh(\psi(s)) & \cosh(\psi(s)) \end{pmatrix}, \quad (2.20)$$

leaves the metric η_{AB} unvaried. Under this transformation, the torsion (2.2) behaves as a gauge connection [13,23,24]

$$\tau(s) \to \tau(s) + \partial_s\psi(s). \quad (2.21)$$

Hence, if the functional (1.5) is evaluated on an open curve, it is not necessarily invariant under gauge transformations. Instead it picks up end point contributions

$$\mathcal{F}[\gamma] \to \mathcal{F}[\gamma] + \mathfrak{s}[\psi(s_f) - \psi(s_i)], \quad (2.22)$$

in a manner analogous to a Chern-Simons action. The crucial consequence of this observation is that to find a unique on-shell value for (1.5) it is not sufficient to fix boundary conditions for the curve but it is also necessary to impose conditions on the normal vectors. In accordance to [14] we compel the timelike normal vector to point in a predefined notion of *boundary time* at both end points. If instead we were to calculate the on-shell value for a κ-boosted version of the same curve, while keeping the notion of boundary time fixed, then we would need to adjust the normal frame to satisfy the boundary condition. This adjustment can be implemented by a gauge transformation satisfying $\psi(s) \to -\kappa$ at the curve's end points. Therefore, comparing both results we find that under a global Lorentz boost $\Lambda(\kappa)^\nu{}_\mu$, we have

$$\mathcal{F}[\Lambda(\kappa)\gamma] - \mathcal{F}[\gamma] = -2\mathfrak{s}\kappa, \quad (2.23)$$

which is a manifestation of the quantum violation of boost invariance: a gravitational anomaly.

We stress that the shape equations (2.3) are gauge covariant [15], and hence the shape of the Mathisson helix itself is independent of the choice of frame. However, as mentioned before, this is not the case for the on-shell value of the functional (1.5). To illustrate this, we consider two different gauge choices: the *Fermi-Walker gauge*, where the torsion is set to zero along the entire curve, and the *Frenet-Serret gauge,* where one of the extrinsic curvatures is set to zero identically. In the Fermi-Walker frame, the on-shell value of (1.5) reads

$$\mathcal{F}_{\mathrm{FW}}[\gamma] = \mathfrak{m}\mathrm{L}[\gamma]. \quad (2.24)$$

In contrast, for the Frenet-Serret frame we find

$$\mathcal{F}_{\mathrm{FS}}[\gamma] = 2\mathfrak{m}\mathrm{L}[\gamma], \quad (2.25)$$

where we made use of Eq. (2.7). Clearly, the Frenet-Serret frame and the Fermi-Walker frame can be related by a gauge transformation. However, this must be a *large* gauge transformation,[2]

[1]Every curve with fixed k_{FS}^2 and τ_{FS} in AdS_3 can be written as the image of an AdS_3 isometry acting on a seed solution; this follows from the fundamental theorem of curves.

[2]See [25] for an interesting discussion on the subject of gauge transformations and boundary conditions.

$$\psi \sim \left(\frac{\mathfrak{m}}{\mathfrak{s}}\right) s, \tag{2.26}$$

where s is the arclength parameter. Intuitively, this means that to go from the Frenet-Serret to the Fermi-Walker frame we must *unwind* the normal frame an infinite number of times. In both cases, the answer is proportional to the length of the helix γ, which is given by

$$\mathrm{L}[\gamma] = \frac{2}{\lambda_+}\log\left(\frac{\ell}{\epsilon}\right), \tag{2.27}$$

where ℓ is the length of the boundary interval, λ_+ is a helix parameter, and ϵ is an ultraviolet cutoff. It is straightforward to check that in order to obtain the right value for the CFT computation, we must choose the Fermi-Walker frame and $\lambda_+ = 1/L$. The latter requirement implies that choosing geodesics as the extremal curve yields the right answer. In view of this fact, the reader might think that nongeodesic Mathisson's helices play no role in the study of entanglement entropy. Nonetheless, this would be a premature conclusion as we shall see in the next section.

III. HOLOGRAPHIC RG FLOWS

In the previous section we introduced the shape equations (2.3) and discussed some of their general properties in AdS_3 spacetime. We found that any pair of spacelike separated boundary points can be connected using Mathisson's helix, which could be a geodesic. Now, we consider conformally flat ambient geometries which approach AdS_3 asymptotically:

$$ds^2 = \frac{L_{\mathrm{UV}}^2}{z^2}\left(\eta_{ab}dx^a dx^b + \frac{dz^2}{f(z)^2}\right), \tag{3.1}$$

with $f(z) \to 1$ as $z \to 0$. These spacetimes are known to provide a holographic description of the behavior of renormalization group flows [26]. The infrared ($z \to \infty$) behavior of these metrics is

$$\mathrm{CFT}_{\mathrm{UV}} \to \mathrm{CFT}_{\mathrm{IR}}, \quad \text{for which } f(z) \to L_{\mathrm{UV}}/L_{\mathrm{IR}}. \tag{3.2}$$

Spacetimes of this form are studied in detail in [27]; see also Appendix C. Our task now is to learn how to connect spacelike separated boundary points via Mathisson helices.

We view these metrics as solutions to the equations of motion of TMG [4] coupled to a scalar field,

$$R_{\mu\nu} - \frac{1}{2}g_{\mu\nu}R + \frac{1}{\mu}C_{\mu\nu} = 8\partial_\mu\varphi\partial_\nu\varphi - 4g_{\mu\nu}\partial^\lambda\varphi\partial_\lambda\varphi - \frac{1}{2}g_{\mu\nu}V(\varphi), \tag{3.3}$$

where

$$C_{\mu\nu} = \epsilon_\mu{}^{\lambda\sigma}\nabla_\lambda\left(R_{\sigma\nu} - \frac{1}{4}g_{\sigma\nu}R\right) \tag{3.4}$$

is the Cotton-York tensor. The Cotton-York tensor vanishes for conformally flat geometries; thus, in practice Eqs. (3.3) reduce to Einstein's equations. Nevertheless, we insist on regarding (3.1) in the context of TMG because the Brown-Henneaux analysis of this theory yields the central charges [5]

$$c_L = \frac{3L}{2G_3}\left(1 - \frac{1}{\mu L}\right), \qquad c_R = \frac{3L}{2G_3}\left(1 + \frac{1}{\mu L}\right), \tag{3.5}$$

which signals the presence of the gravitational anomaly. In terms of the TMG couplings, the coefficients of the entangling functional (1.5) are given by

$$\mathfrak{m} = \frac{1}{4G_3}, \qquad \mathfrak{s} = \frac{1}{4G_3\mu}, \tag{3.6}$$

as demonstrated in [14].

For an interpolating geometry of the form (3.1), the coupling between the ambient curvature and the moving frame reads

$$R_s{}^A = \frac{f'(z)}{zf(z)}n^{Az}t^z, \tag{3.7}$$

which together with (2.6) implies that k_{FS}^2 is not necessarily constant along Mathisson helices. Hence, in contrast to the AdS_3 case, it is uncertain whether every geodesic in (3.1) can be regarded as a Mathisson helix. Indeed, since both extrinsic curvatures k^A must vanish along geodesics, for them to solve Eq. (2.3) we must have $R_s{}^A = 0$, which implies that either $t_s^z = 0$ or $n^{Az} = 0$. The first instance corresponds to a curve with a constant z component, that is, a curve lying on a plane parallel to the boundary. In the second case, both normal vectors are orthogonal to the z direction, which implies that the tangent vector itself is orthogonal to the boundary. Neither of these kinds of geodesics can be used to connect spacelike separated points in the boundary, the former being unable to reach the boundary and the latter touching the boundary only at one point. We conclude that to connect boundary points we are compelled to use nongeodesic Mathisson helices. Moreover, as these helices approach the boundary they should approximate either (2.15) or (2.16), up to isometries.

IV. RENORMALIZED LENGTH-TORSION FUNCTIONAL

Consider the set of spacelike boundary intervals with fixed rapidity κ and arbitrary Lorentz-invariant length ℓ in the spacetime (3.1). Assume that a prescription to construct a unique Mathisson helix $\gamma(\ell)$ connecting the end points

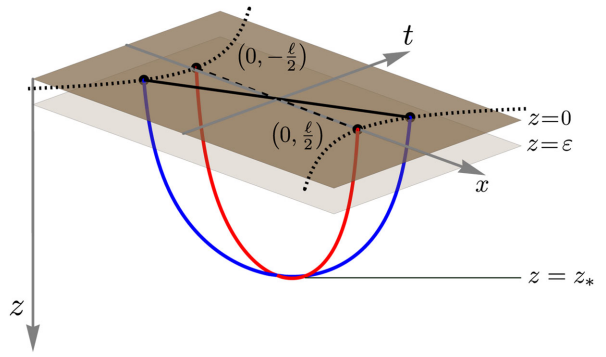

FIG. 1. In the Poincaré patch of asymptotically AdS_3 spacetimes, we study curves which admit a *tip* z_*, i.e., a point where $\dot{z}=0$ and $\ddot{z}<0$. We show two curves with identical z_* but different ζ_*: this corresponds to a rigid boost, and hence the end points of the red curve lie on the $t=0$ line, while the blue curve end points are boosted. In numerical solutions, boundary quantities, such as ℓ and the boost κ, are computed at $z(\pm s_\epsilon)=\epsilon$.

of each of such intervals has been provided; see Fig. 1. The question we wish to address is, how does the renormalized functional

$$\hat{\mathcal{F}}[\gamma(\ell)]=\ell\frac{\partial}{\partial\ell}\mathcal{F}[\gamma(\ell)] \tag{4.1}$$

behave as a function of ℓ? To make progress, it is convenient to express the functional (1.5) in terms of a Lagrangian density as

$$\mathcal{F}[\gamma(\ell)]=\int_{-s_\epsilon(\ell)}^{s_\epsilon(\ell)}ds\mathcal{L}[\gamma(\ell)], \tag{4.2}$$

with $s_\epsilon(\ell)$ defined by requiring

$$z(\pm s_\epsilon(\ell))=\epsilon, \tag{4.3}$$

where ϵ is an ℓ-independent ultraviolet cutoff. We denote by $(T_\pm,X_\pm)$ the end points of the interval, which satisfy

$$T_+-T_-=\ell\sinh\kappa,\qquad X_+-X_-=\ell\cosh\kappa, \tag{4.4}$$

by definition.

The advantage of expressing the functional (1.5) in the form (4.2) is that the ℓ-derivative of $\mathcal{F}[\gamma(\ell)]$ can be separated into two distinct contributions

$$\frac{\partial\mathcal{F}}{\partial\ell}=\frac{\delta\mathcal{F}}{\delta\gamma_\mu}\frac{\partial\gamma_\mu}{\partial\ell}+\frac{\partial s_\epsilon}{\partial\ell}\mathcal{L}[\gamma(\ell)]\Big|_{-s_\epsilon}^{+s_\epsilon}. \tag{4.5}$$

The first term follows from the variation of $\mathcal{F}$ under $\gamma^\mu\to\gamma^\mu+\delta\gamma^\mu$, which can be written as

$$\delta\mathcal{F}[\gamma]=\int_\gamma ds[\mathcal{E}^\mu\delta\gamma_\mu+\partial_s(\mathcal{J}^\mu\delta\gamma_\mu)], \tag{4.6}$$

the explicit forms of $\mathcal{E}^\mu$ and $\mathcal{J}^\mu$ can be found in Eq. (A5); for the present argument only some of their general properties are required. For instance, we will use the fact that $t_\mu\mathcal{E}^\mu$ vanishes identically and that requiring

$$n_\mu^A\mathcal{E}^\mu=0 \tag{4.7}$$

is equivalent to the shape equations (2.3). Hence, since we are considering the variation of the functional about a Mathisson helix, the first term in the right-hand side of (4.6) vanishes. Moreover, given that tangential variations of the functional correspond to reparametrizations of the curve, then

$$\mathcal{J}^\mu t_\mu=\mathcal{L}. \tag{4.8}$$

Thus, we can write (4.5) as

$$\frac{\partial\mathcal{F}}{\partial\ell}=\left[\mathcal{J}_\mu\left(t^\mu\frac{\partial s_\epsilon}{\partial\ell}+\frac{\partial\gamma^\mu}{\partial\ell}\right)\right]_{-s_\epsilon}^{+s_\epsilon}. \tag{4.9}$$

Furthermore, the end point values of z (which are equal to the cutoff ϵ) are independent of ℓ. Consequently,

$$\left.\frac{dz}{d\ell}\right|_{\pm s_\epsilon}=\left[\dot{z}\frac{\partial s_\epsilon}{\partial\ell}+\frac{\partial z}{\partial\ell}\right]_{\pm s_\epsilon}=0, \tag{4.10}$$

Eq. (4.9) becomes

$$\frac{\partial\mathcal{F}}{\partial\ell}=\left[\mathcal{J}_\mu\left(\frac{\partial\gamma^\mu}{\partial\ell}-\frac{\dot{\gamma}^\mu}{\dot{z}}\frac{\partial z}{\partial\ell}\right)\right]_{-s_\epsilon}^{+s_\epsilon}, \tag{4.11}$$

and it is no longer necessary to compute derivatives of s_ϵ.

Notice that as the helix γ reaches toward any of its end points, its shape asymptotizes to one of the AdS_3 helices described in Sec. II A. Interestingly, the asymptotic helices approached at each end point might be distinct. As shown in Appendix D, the vector

$$\left(\frac{\partial\gamma^\mu}{\partial\ell}-\frac{\dot{\gamma}^\mu}{\dot{z}}\frac{\partial z}{\partial\ell}\right), \tag{4.12}$$

evaluated on an AdS_3 helix becomes a Killing vector which generates spacetime translations in (3.1). Variations taken along any Killing direction ξ_μ must leave the functional invariant; hence it follows from Eq. (4.6) that $\mathcal{J}^\mu\xi_\mu$ is a conserved quantity. As a matter of fact, in Appendix B we demonstrate that it matches the spinning-body conserved charge $\mathcal{Q}_\xi[\gamma]$ in Eq. (2.12). Bringing these facts together, it follows that the charges are bound to emerge from the contraction inside the bracket in (4.11). Finally, after dealing with a few technical details which can be found in Appendix D, we obtain the elegant expression

$$\hat{\mathcal{F}}[\gamma(\ell)] = \ell(\mathcal{Q}_t[\gamma]\sinh\kappa + \mathcal{Q}_x[\gamma]\cosh\kappa), \tag{4.13}$$

where $\mathcal{Q}_t[\gamma]$ and $\mathcal{Q}_x[\gamma]$ are the Noether charges associated with space and time translations, respectively. In particular, setting $\kappa = 0$ we have

$$\hat{\mathcal{F}}[\gamma(\ell)] = \ell\mathcal{Q}_x[\gamma], \tag{4.14}$$

which in the limit $\mathfrak{s} \to 0$ reduces to the entropic c-function constructed in [10]. Besides translational symmetries, note that the metric (3.1) is also endowed with boost invariance. This leads to an additional Noether charge

$$\mathcal{Q}_b[\gamma] = x\mathcal{Q}_t[\gamma] + t\mathcal{Q}_x[\gamma] + \mathfrak{s}\frac{\dot{z}}{zf(z)}. \tag{4.15}$$

Interestingly, for curves that reach the asymptotic AdS boundary, and thus are Mathisson helices of the type discussed in Sec. II A, the last term is always equal to $\mathfrak{s}\lambda_+$. In the following section we will show that the relevant solutions have $\mathcal{Q}_b[\gamma] = 0$ and from the conservation of this quantity it follows that

$$\hat{\mathcal{F}}[\gamma(\ell)] = \mathfrak{s}\lambda_+\left(\frac{\mathcal{Q}_x[\gamma]}{\mathcal{Q}_t[\gamma]}\right), \tag{4.16}$$

provided $\mathfrak{s} \neq 0$.

V. MATHISSON HELICES: EXPLICIT PARAMETRIZATION

In this section we provide an explicit parametrization to construct the Mathisson helices in an ambient spacetime of the form (3.1). In the case of AdS_3, the shape equations (2.3) can be solved following a two-step procedure. First, we solve (2.3) for the extrinsic quantities k^A and τ and with these results in hand we then construct the actual curves [15]. Due to the nontrivial coupling of the moving frame with the ambient curvature (3.7), this procedure cannot be applied in the case of (3.1), and we are forced to introduce an explicit parametrization for the curve. As a matter of fact, the best procedure is to introduce a parametrization such that the tangent vector is automatically normalized, so that the resulting curve is parametrized by arclength. Thus, we introduce functions $\zeta(s)$ and $\delta(s)$ such that the tangent vector reads

$$t^\mu = \frac{z}{L_{\rm UV}}\begin{pmatrix}\sinh\zeta\\ \cos\delta\cosh\zeta\\ f(z)\sin\delta\cosh\zeta\end{pmatrix}. \tag{5.1}$$

Using (3.1) it is straightforward to verify that $t^\mu t_\mu = 1$. Next, we construct the normal frame by inverting Eqs. (2.1). Due to the gauge degeneracy in the normal bundle, we must fix a gauge beforehand in order to find a unique solution. We fix the gauge by demanding that $n^{1t} = 0$ and obtain

$$n^{1\mu} = \frac{z}{L_{\rm UV}}\begin{pmatrix}0\\ \sin\delta\\ -f(z)\cos\delta\end{pmatrix},$$
$$n^{2\mu} = \frac{z}{L_{\rm UV}}\begin{pmatrix}\cosh\zeta\\ \cos\delta\sinh\zeta\\ f(z)\sin\delta\sinh\zeta\end{pmatrix}, \tag{5.2}$$

for which $\eta_{AB} = \mathrm{diag}(1,-1)$. In this frame, the curvatures and torsion read

$$k^1 = \frac{f(z)}{L_{\rm UV}}\cos\delta + \dot{\delta}\cosh\zeta,$$
$$k^2 = \dot{\zeta} - \frac{f(z)}{L_{\rm UV}}\sin\delta\sinh\zeta, \qquad \tau = -\dot{\delta}\sinh\zeta, \tag{5.3}$$

and the shape equations (2.3) can be written as

$$\mathfrak{m}\left(\frac{f(z)}{L_{\rm UV}}\cos\delta + \dot{\delta}\cosh\zeta\right) + \mathfrak{s}\left[\ddot{\zeta} + \cosh\zeta\left(\dot{\delta}^2\sinh\zeta - \frac{f(z)}{L_{\rm UV}}\dot{\zeta}\sin\delta\right)\right] = 0, \tag{5.4}$$

$$\mathfrak{m}\left(\frac{f(z)}{L_{\rm UV}}\sin\delta\sinh\zeta - \dot{\zeta}\right) + \mathfrak{s}\left[-\cosh\zeta\ddot{\delta} + \dot{\delta}\left(\frac{f(z)}{L_{\rm UV}}\sin\delta\cosh^2\zeta - 2\dot{\zeta}\sinh\zeta\right)\right] = 0. \tag{5.5}$$

These equations, together with the third component of the tangent vector (5.1) make up a closed system of ordinary differential equations for $\zeta(s)$, $\delta(s)$, and $z(s)$. The x and t coordinates of the curve can be obtained by integrating the respective components of (5.1).

We construct the Mathisson helices by integrating the system of equations presented above using the *shooting method*. We choose a point in the bulk $\gamma^\mu(0) = (t_*, x_*, z_*)$ where $\dot{z}(0) = 0$, which we call the tip, from which we follow the curve going toward the boundary. Observe that from (5.1) it follows that $\delta(0) = 0$. Using translational invariance we set $t_* = x_* = 0$. Clearly, these conditions are not sufficient to fix a unique solution to the shape equations, and additionally we must provide a set of *shooting conditions*,

$$\{\zeta_*, \dot{\delta}_*, \dot{\zeta_*}\}, \tag{5.6}$$

at any depth z_*, where the asterisk subscript indicates that the quantity is being evaluated at $s = 0$. Alternatively, we can use the values of the extrinsic curvatures

$$\{\zeta_*, k_*^1, k_*^2\} \tag{5.7}$$

as shooting conditions. The data (5.6) and (5.7) can be translated into one another using

$$k_*^1 = \frac{f_*}{L_{\rm UV}} + \dot{\delta}_* \cosh\zeta_*, \qquad k_*^2 = \dot{\zeta}_*. \tag{5.8}$$

In contrast to geodesics where only two parameters, depth and orientation, are needed to fix a unique solution, for Mathisson helices we must provide four. As discussed in Sec. IV, we are interested in helices that connect the end points of spacelike intervals. It is important to bear in mind that at any given depth z_*, only certain choices of shooting conditions will generate a helix that reaches the boundary in this fashion. We say that those conditions belong to the *escape region* of the model. We shall see some examples of these regions in Sec. V A.

In the parametrization (5.1), the spinning-body Noether charges (2.12) are given by

$$\mathcal{Q}_t = -\frac{L_{\rm UV}}{z}(\mathfrak{m}\sinh\zeta + \mathfrak{s}\dot{\delta}\cosh^2\zeta), \tag{5.9}$$

$$\mathcal{Q}_x = \frac{L_{\rm UV}}{z}[\mathfrak{m}\cos\delta\cosh\zeta + \mathfrak{s}(\dot{\delta}\cos\delta\cosh\zeta\sinh\zeta - \dot{\zeta}\sin\delta)] \tag{5.10}$$

for translational symmetries and

$$\mathcal{Q}_b = x\mathcal{Q}_t + t\mathcal{Q}_x + \mathfrak{s}\sin\delta\cosh\zeta \tag{5.11}$$

for boosts on the (t, x) plane. By evaluating these charges at the tip, we immediately see that $\mathcal{Q}_b = 0$, while the translational charges can be written as

$$\begin{pmatrix}\mathcal{Q}_t\\ \mathcal{Q}_x\end{pmatrix} = \frac{L_{\rm UV}}{z_*}\begin{pmatrix}\cosh\zeta_* & -\sinh\zeta_*\\ -\sinh\zeta_* & \cosh\zeta_*\end{pmatrix}\begin{pmatrix}\mathfrak{s}(f_*/L_{\rm UV} - k_*^1)\\ \mathfrak{m}\end{pmatrix}. \tag{5.12}$$

A. Helical motions: Numerical solutions

In this section we highlight the results from the systematic numerical study of the shape equations performed on backgrounds of the form (3.1) [and (C2)]. We construct numerical solutions for the system of equations (5.1), (5.4), and (5.5) parametrized by $\mathfrak{m}$, $\mathfrak{s}$, the tip depth z_*, the shooting conditions $\{\zeta_*, k_*^1, k_*^2\}$, and the parameters that determine the warp factor $f(z)$. We produce five interpolating functions,

$$\{t(s), x(s), z(s), \delta(s), \zeta(s)\}, \tag{5.13}$$

and check whether γ reaches the asymptotic boundary. Since the spacetime is asymptotically AdS_3, the solutions will necessarily approach either a I_a or a I_c Mathisson helix, as we showed in Sec. II A. Each solution is unique once we fix initial conditions and parameters. In fact, we can lower the number of degrees of freedom of the solutions by imposing a few extra requirements. The first requirement is that γ should approach the *same* type of Mathisson helix on both end points; i.e., the solution should have identical values of $\lambda_\pm$ asymptotically. This is equivalent in requiring that the solution should be symmetric under the change of arclength parameter $s \to -s$, and it is easy to see that this is obtained only if $k_*^2 = 0$. Some examples of escape regions satisfying this condition are given in Fig. 2. Then, in order for (4.13) to hold, all curves we consider should also have identical κ; without loss of generality we can set $\kappa = 0$, so both end points lie in the

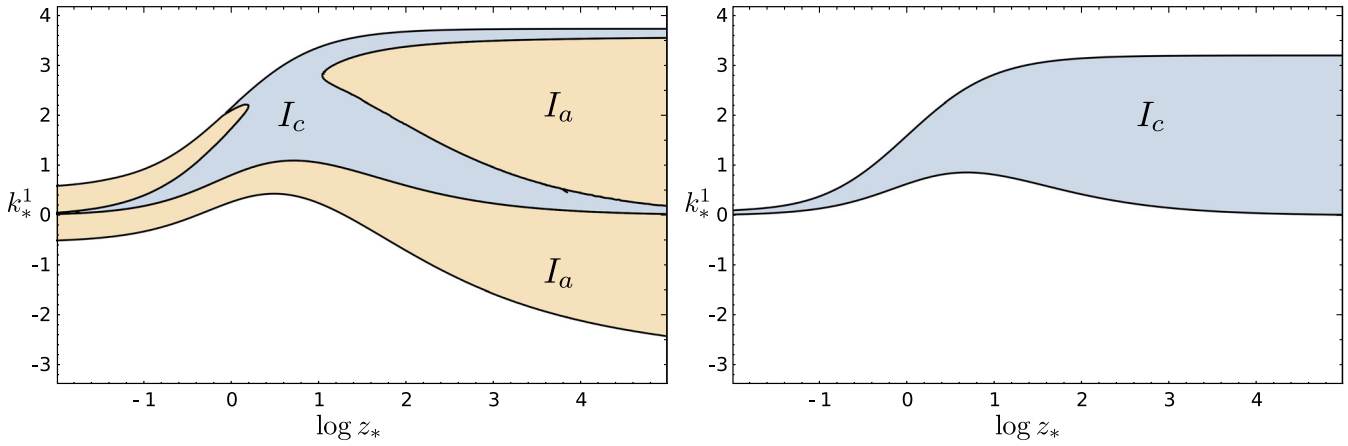

FIG. 2. Example of escape regions: in the tip parameter space (z_*, k_*^1), we show which values allow for a boundary-reaching solution. The blue/yellow color coding stands for the I_a and I_c helix types, described in (2.15) and (2.16). In both plots we set $L_{\rm UV}/L_{\rm IR} = 1/4$, $\mathfrak{m} = 1$, $\zeta_* = 0$, $\dot{\zeta}_* = 0$. We used the interpolating function $f(z)$ in (C1). The left panel has $\mathfrak{s} = 2$, while the right one has $\mathfrak{s} = 1$. Since for the latter $\mathfrak{m}/\mathfrak{s} = 1/L_{\rm UV}$, it represents the chiral point of the theory: notice the absence of type I_a asymptotic behavior.

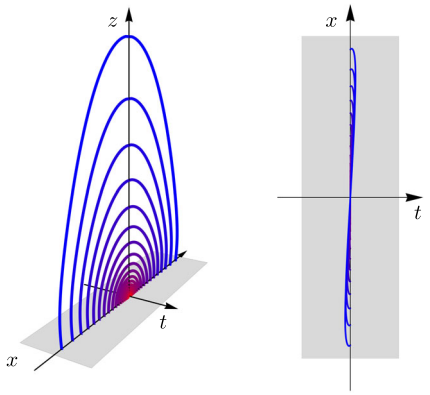

FIG. 3. Graphical representation of a family of Mathisson helices, solutions of Eqs. (5.4) and (5.5). The color of each curve ranges from red to blue as z_* is increased. This family is such that the boundary interval boost, κ, vanishes (i.e., the end points lie on the $t = 0$ line) and the asymptotic total curvature k^2_{FS} is zero on both end points. These curves are *not* geodesics, and they are nonplanar: the vertical view on the right shows this unequivocally. Note that the boundary conditions $\kappa = 0$ and $\lambda_+ = 1$ can be reached only with a specific choice of tip values ζ_* and k^1_*. This choice changes nontrivially for different z_*.

$t = 0$ slice. Satisfying this condition imposes a nontrivial relationship between the three remaining tip quantities (ζ_*, z_*, and k^1_*), which we are able to find numerically as a specific value of ζ_* for fixed z_* and k^1_*. Only after this condition is imposed, to each point in the escape region corresponds one and only one Mathisson helix. For every Mathisson helix, we then compute $\ell(z_*, k^1_*)$ and $\hat{\mathcal{F}}(z_*, k^1_*)$. The final outputs of our algorithm are the values of these quantities within the escape regions; we present some examples in Figs. 4 and 5.

Based on these findings we would like to construct *entropic c*-functions out of Mathisson's helices. Attaining this involves selecting a suitable family of Mathisson helices; in practice this corresponds to delineating a properly chosen trajectory within the (z_*, k^1_*) plane. First of all, we require that this trajectory relates monotonically the depth z_* with the boundary width ℓ, which yields a family of curves as the one depicted in Fig. 3. Furthermore, we demand this trajectory to reproduce the expected CFT values

$$c_{\mathrm{UV}} = 6\mathfrak{m}L_{\mathrm{UV}} \quad \text{and} \quad c_{\mathrm{IR}} = 6\mathfrak{m}L_{\mathrm{IR}} \tag{5.14}$$

as $z_* \to 0$ and $z_* \to \infty$, respectively, and to interpolate between these monotonically. This means that we must select a trajectory with $k^1_* \to 0$ in the UV as well as at the IR. This trajectory must cross each contour in both plots in Fig. 4 once and only once. In general there are infinitely many ways of attaining this. However, at the chiral point, where $\mathfrak{m}/\mathfrak{s} = 1/L_{\mathrm{UV}}$, the contours behave in a different manner (see Fig. 5): they either intersect the lower boundary of the escape region or continue freely toward the IR, the critical value between these two cases precisely being the contour corresponding to the expected CFT value in the IR. Clearly, monotonicity requires that our trajectory remains below that contour. From our numerical results, we notice that as we increase the ratio $L_{\mathrm{UV}}/L_{\mathrm{IR}}$, the critical contour comes closer to the lower boundary of the escape region. Therefore, if we want to have a general prescription, we must make our trajectory match the lower boundary of the escape region; this corresponds to a family of asymptotically geodesic Mathisson helices. While this choice is clearly a necessary condition for monotonicity, it does not guarantee it. However, we also considered other geometries in Appendix C and obtained qualitatively similar results (compare Fig. 5 with Fig. 6 in the Appendix C). Thus, we propose an entropic *c*-function

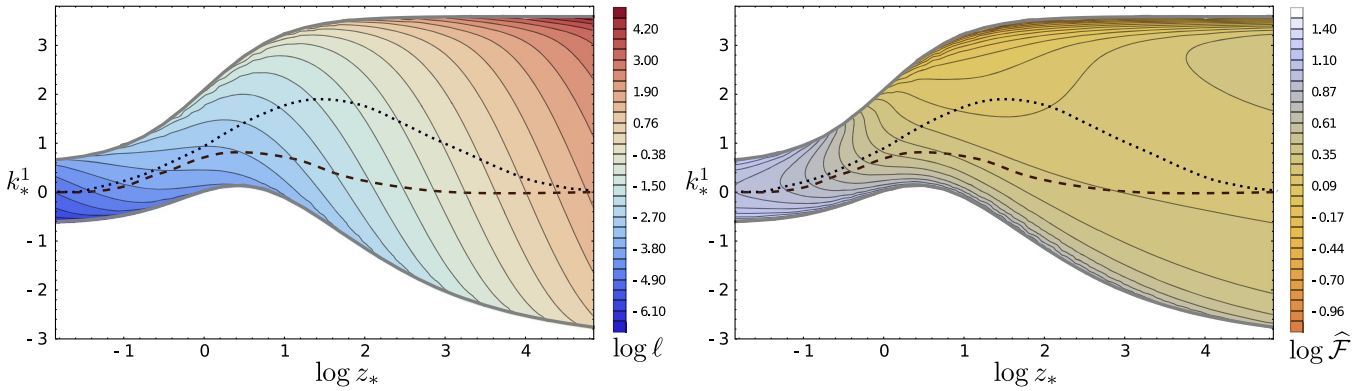

FIG. 4. We take the escape region in the left panel of Fig. 2 and plot logarithmic contour lines $\ell(z_*, k^1_*)$ (on the left) and $\hat{\mathcal{F}}(z_*, k^1_*)$ (on the right). For each point within the region, we carefully tuned ζ_* so that each Mathisson helix ends at the boundary with $\kappa = 0$, as in Fig. 3. Within the escape region we also show two black lines, as exemplification of possible choices for curve prescriptions. The dashed (lower) black line corresponds to a prescription which as we change ℓ is also monotonic in $\hat{\mathcal{F}}$. On the other hand, the dotted black line is an unsuitable choice because for increasing ℓ, the value of $\hat{\mathcal{F}}$ decreases (this happens where the line crosses the same contour twice).

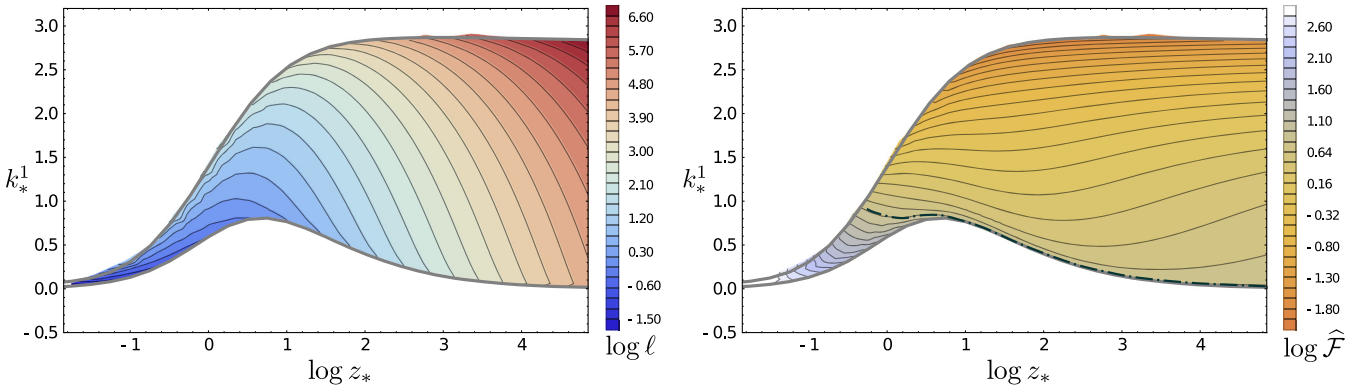

FIG. 5. The escape region at the chiral point, taken from the right panel of Fig. 2, with logarithmic contour lines of $\ell(z_*, k_*^1)$ (on the left) and $\hat{\mathcal{F}}(z_*, k_*^1)$ (on the right). The vertical axis has been rescaled with respect to Fig. 2. The dot-dashed black line in the right panel shows the critical contour discussed in the main text. The value of $\hat{\mathcal{F}}$ along this line is precisely the infrared CFT value of the central charge: therefore, monotonicity requires that any asymptotic prescription must lie below this limiting contour.

$$\frac{c_{\mathrm{Hel}}(\ell)}{3} = \frac{\mathcal{Q}_x}{\mathcal{Q}_t}, \tag{5.15}$$

at the chiral point based on the renormalized EE functional (1.5) and which can be computed entirely in terms of spinning body conserved charges. Even though the curves used to compute (5.15) are asymptotically geodesic, it is important to point out that this quantity is different from the nonanomalous case ($\mathfrak{s} = 0$). In fact, using (4.14) and the charges (5.12), we can write

$$\hat{\mathcal{F}} = L_{\mathrm{UV}}\left(\frac{\ell}{z_*}\right)[\mathfrak{s}\sinh(\zeta_*)(k_*^1 - f_*/L_{\mathrm{UV}}) + \mathfrak{m}\cosh(\zeta_*)]. \tag{5.16}$$

In the nonanomalous case, extremal curves are geodesics with $\zeta_* = 0$; hence

$$\hat{\mathcal{F}} = \frac{c_{\mathrm{Geo}}(\ell)}{3} = \mathfrak{m}L_{\mathrm{UV}}\left(\frac{\ell}{z_*}\right), \tag{5.17}$$

which is precisely the result found in [10].

VI. DISCUSSION AND OUTLOOK

In this work we have explored the physical properties of the length-torsion functional (1.5). As demonstrated in [14], this functional computes holographically the entanglement entropy for $(1+1)$-dimensional theories with chiral anomalies. Moreover, in a previous paper [15] we have shown that the extremal curves of this functional correspond to Mathisson's helical motions for the centers of mass of spinning bodies. Here, we have brought together these two points of view and constructed an entropic c-function $c_{\mathrm{Hel}}(\ell)$ which can be written in terms of Noether charges along Mathisson's helices. While for generic values of the anomaly there is some ambiguity in the definition of $c_{\mathrm{Hel}}(\ell)$, we argue that at the chiral point (1.1) this ambiguity is absent: we find the succinct expression (5.15), which must be evaluated on asymptotically geodesic Mathisson helices. While we have gathered extensive numerical evidence in support of the monotonicity of this function, we leave the derivation of a formal proof of this fact for future work.

We wish to point out that the steps leading to the expressions for the renormalized functional, Eqs. (4.13) and (4.16), relied only on the assumption of having an AdS_3 asymptopia. Hence, these expressions can be used without any modification for any IR behavior one might wish to study, such as warped AdS_3, Janus, or gapped geometries. Indeed, for the case of gapped geometries we will detail in a forthcoming work how Mathisson helices prevent the formation of mass gaps which are precluded by anomaly matching; see [28] for a general argument. Another intriguing direction is to revisit entanglement entropy for theories with different symmetry algebras and whose gravitational duals are naturally understood in the realm of TMG such as Galilean CFTs; see for instance [29,30]. On a more ludic note, when exploring the space of Mathisson helices in domain walls, we noticed that beyond the escape regions of Fig. 2, there are also extra, small regions in the parameter space which correspond to a curious kind of solution: curves in these regions escape toward the boundary only after traveling deeper into the bulk and gathering enough momentum from the spin-curvature interaction. The tip z_*, for these curves, is only a local maximum of $z(s)$. It would be amusing to explore what these solutions might be able to teach us. Finally, we wish to understand the results discussed in this work from a field theoretic standpoint. First, it would be desirable to obtain a CFT picture of Mathisson's helices and their charges. Based on this, we ought to be able to translate $c_{\mathrm{Hel}}(\ell)$ into the language of the dual theory. Presumably, this would allow us to make contact with the very interesting

literature concerning EE in CFTs with chiral anomalies [31–34].

ACKNOWLEDGMENTS

P. F. is supported by the Netherlands Organisation for Scientific Research (NWO/OCW). The work of A. V. O. is supported by NCN Grant No. 2012/06/A/ST2/00396. A. V. O. thanks the Yukawa Institute for Theoretical Physics for hospitality during the development of this work. Also, A. V. O. is grateful to Abdus Salam International Center for Theoretical Physics where he carried out some of the final stages of this project. It is a pleasure to acknowledge Michael Abbott, Paweł Caputa, Alejandra Castro, Filipe Costa, Mario Flory, Vishnu Jejjala, and José Natario for enlightening conversations and correspondence. We thank Alejandra Castro, Mario Flory, Vishnu Jejjala, and Hesam Soltanpanahi for helpful comments on earlier versions of this work. Especially, we wish to express our gratitude to Alejandra Castro for suggesting we look into these questions.

APPENDIX A: HELICAL NOETHER CHARGES

In this Appendix we show how the quantity (2.12) can be derived from the action (1.5) by means of Noether's theorem.

Since $\{t^\mu, n^{1\mu}, n^{2\mu}\}$ form an oriented basis frame in the neighborhood of the curve, we can decompose any (Killing) vector field ξ^μ defined on TM in its components. Explicitly we have

$$\xi^\mu = \xi_t t^\mu + \xi_A n^{A\mu}, \tag{A1}$$

where ξ_t and ξ_A are, respectively, the tangential and normal components of the Killing vector field.

Note that the expression written in (2.12) is gauge invariant; i.e., it does not depend on any particular choice of the curve's normal frame. For this reason, it is convenient to (temporarily) make (1.5) also gauge invariant by adding a *compensator*,

$$\tilde{\mathcal{F}}[\gamma] \equiv \int_\Sigma ds(\mathfrak{m} + \mathfrak{s}(\tau - \dot{\psi})), \tag{A2}$$

where $\psi(s)$ is the hyperbolic angle of $n^{1\mu}$ with any arbitrarily fixed normal frame. For example, we can choose ψ to be the angle with the Fermi-Walker gauge choice, so that *if and only if* we compute geometrical quantities in this frame, we can set $\psi = 0$. Under a local frame rotation the compensator term changes in exactly the opposite way as τ, rendering (A2) effectively gauge invariant. The compensator arises also in the evaluation of some connection forms, namely

$$\frac{1}{2}\epsilon_{AB} n^{A\mu} n^{B\nu} \nabla_\mu t_\nu = \tau - \dot{\psi}, \tag{A3}$$

the left-hand side of this expression being a well-behaved scalar.

We can now substitute (A1) into (2.12), finding

$$\mathcal{Q}_\xi[\gamma] = \xi_t(\mathfrak{m} + \mathfrak{s}(\tau - \dot{\psi})) - \mathfrak{s}\epsilon_{AB}\left(\xi^A \mathrm{Tr} K^B + \frac{1}{2} n^{A\mu}\nabla_\mu \xi^B + \frac{1}{2}\xi_C \Theta^{ACB}\right). \tag{A4}$$

On the other hand, by taking an on-shell Lie derivative of (A2) along the vector field (A1), we get

$$\mathcal{L}_\xi \tilde{\mathcal{F}}[\gamma] = \left[\xi_t(\mathfrak{m} + \mathfrak{s}(\tau - \dot{\psi})) - \mathfrak{s}\epsilon_{AB}\left(\xi^A \mathrm{Tr} K^B - \frac{1}{2}\xi_C \Theta^{CBA}\right)\right]_{s=\pm\infty}. \tag{A5}$$

To obtain the above result we used the fact that the bulk of the variation is zero because of the shape equations, and we used the fact that $\mathcal{L}_\xi \psi = 0$ at the boundary. Because of Noether's theorem, if ξ^μ is a Killing vector field, with (A2) a geometrical invariant action (i.e., it does not depend on coordinate choices), then the term inside the brackets of (A5) and expression (A4) should match.

In order to prove the equivalence of the two expressions, we need to use the fact that Killing vectors preserve orthonormal frames. In particular, the normal vectors can be Lie-transported along any spacetime Killing directions

$$\mathcal{L}_\xi n^{B\mu} = \xi^\nu \nabla_\nu n^{B\mu} - n^{B\nu}\nabla_\nu \xi^\mu = 0. \tag{A6}$$

By contracting the above expression with $\epsilon_{AB} n^A_\nu$ we get the relation

$$\epsilon_{AB}(\xi_C \Theta^{CAB} - n^{A\mu}\nabla_\mu \xi^B - \xi_C \Theta^{ACB}) = 0, \tag{A7}$$

which, upon using $\xi_C \Theta^{C[AB]} = 0$, proves the equivalence between (A4) and (A5).

APPENDIX B: SPINNING-BODY CHARGES IN AdS_3

In the following, we compute the conserved charges of helices isometric to (2.15) or (2.16) in AdS_3 (here, the AdS radius is equal to L). Specifically, we are interested in helices of the form

$$\gamma^\mu(s) = \frac{r}{2L} M^\mu{}_\nu x^\nu(s) + \Delta^\mu, \tag{B1}$$

where x^ν is either $\gamma^\mu_{I_a}$ [see (2.15)] or $\gamma^\mu_{I_c}$ [see (2.16)]. The coefficient $r/2L_{\mathrm{UV}}$ sets the boundary interval length to $\ell = r$, while M^μ_ν and Δ^μ are, respectively, a rigid boost and a translation

$$M^{\mu}{}_{\nu} = \begin{pmatrix} \cosh\eta & -\sinh\eta & 0 \\ -\sinh\eta & \cosh\eta & 0 \\ 0 & 0 & 1 \end{pmatrix}, \qquad \Delta^{\mu} = \begin{pmatrix} \Delta^t \\ \Delta^x \\ 0 \end{pmatrix}. \tag{B2}$$

A simple approach to compute the Noether charges onto (B1) is to regard the ambient space as a hypersurface embedded in a four-dimensional flat space described as the zero set of $y^{\alpha}y_{\alpha} + L^2$ in $\mathbb{R}^4$, endowed with the metric $\mathrm{diag}(-,-,+,+)$. The map we use for the embedding is

$$(t, x, z) = \frac{L}{y^1 + y^4}(y^2, y^3, L) \tag{B3}$$

with inverse mapping

$$(y^1, y^2, y^3, y^4) = \frac{1}{2z}(L^2 - t^2 + x^2 + z^2, 2Lt, 2Lx, L^2 + t^2 - x^2 - z^2). \tag{B4}$$

In these coordinates, the Killing vectors in $\mathbb{R}^{2,2}$ associated with translations and boost are, respectively,

$$\xi^{\mu}_t = \frac{1}{L}(-y^2, y^1 + y^4, 0, y^2), \tag{B5}$$

$$\xi^{\mu}_x = \frac{1}{L}(y^3, 0, y^1 + y^4, -y^3), \tag{B6}$$

$$\xi^{\mu}_b = \frac{1}{L}(0, y^3, y^2, 0). \tag{B7}$$

To compute $\mathcal{Q}_t$ and $\mathcal{Q}_x$ we use the Frenet-Serret (FS) frame to first calculate the momentum p^{μ} and spin $S^{\mu\nu}$ of the curve. This is a rather complicated task using the Poincaré coordinates for AdS_3, the main difficulty arising from the fact that $\mathcal{D}_s$, defined in (2.2), is not an ordinary derivative. To circumvent this complication, we compute these quantities in the four-dimensional spacetime. Namely, in $\mathbb{R}^{2,2}$ the FS frame equations are linear due to the fact that the directional derivative is simply by

$$\mathcal{D}_s V^{\alpha} = \partial_s V^{\alpha} + \frac{1}{L^2_{\mathrm{UV}}}(y_{\beta}\partial_s V^{\beta})y^{\alpha}. \tag{B8}$$

This linear realization of the FS equations allowed us to construct all types of hyperbolic helices in [13].

To further simplify the computations, we can momentarily take Δ^{μ} to be zero, since $\mathcal{Q}_t$ and $\mathcal{Q}_x$ cannot depend on the absolute position in the (t, x) plane of the curve. We find

$$\begin{pmatrix} \mathcal{Q}_t \\ \mathcal{Q}_x \end{pmatrix} = \frac{2L}{r}\begin{pmatrix} \cosh\eta & \sinh\eta \\ \sinh\eta & \cosh\eta \end{pmatrix}\begin{pmatrix} \mathfrak{s}\lambda_+ \\ \mathfrak{s}\lambda_- \end{pmatrix}. \tag{B9}$$

To compute $\mathcal{Q}_b$ we make use of the fact that

$$\frac{Lt^z}{zf(z)} = \sin\delta\cosh\zeta, \tag{B10}$$

from which we find, for arbitrary translation parameters Δ^{μ}, that

$$\mathcal{Q}_b = \mathcal{Q}_x\Delta^t + \mathcal{Q}_t\Delta^x. \tag{B11}$$

Since $Q_b = 0$, this equation implies the relation

$$\mathcal{Q}_t\Delta^x = -\mathcal{Q}_x\Delta^t. \tag{B12}$$

APPENDIX C: EXPLICIT HOLOGRAPHIC RG FLOW GEOMETRIES

In the main text we make use of RG flow geometries of the form (3.1), where we did not need to specify the functional of the interpolating function $f(z)$. However, for all numerical purposes it is necessary to choose a specific function. In all solutions involved in Figs. 3–5 we made the explicit choice

$$f(z) = \frac{1 + \frac{L_{\mathrm{UV}}}{L_{\mathrm{IR}}}z^2}{1 + z^2}, \tag{C1}$$

which has the key property of interpolating between 1 for $z \to 0$ and $\frac{L_{\mathrm{UV}}}{L_{\mathrm{IR}}}$ for $z \to +\infty$. Although this $f(z)$ is monotonic, the function (C1) is only a *phenomenological* choice, since it does not descend from any *top-down* model.

For this reason, and also to test our analytical results with other geometries, we repeat the numerical analysis of Sec. V A using a second type of metrics: the analytic domain wall solution of three-dimensional $SO(4) \times SO(4)$ gauged supergravity constructed in [27]. In these solutions, the three-dimensional metrics are all of the form

$$ds^2 = e^{-2A(\rho)}\eta_{ab}dx^a dx^b + d\rho^2, \tag{C2}$$

with

$$A(\rho) = \frac{\alpha}{2\beta}\rho - \frac{1}{2}\log\left[\mathrm{sech}\left(\frac{\rho}{\beta}\right)\right], \tag{C3}$$

where

$$\alpha = \frac{L_{\mathrm{IR}} + L_{\mathrm{UV}}}{L_{\mathrm{UV}} - L_{\mathrm{IR}}}, \qquad \beta = \frac{L_{\mathrm{IR}}L_{\mathrm{UV}}}{L_{\mathrm{UV}} - L_{\mathrm{IR}}}. \tag{C4}$$

Since this geometry is given in a different coordinate patch than Eq. (3.1), for the reader's convenience we reproduce below some of the basic formulas of Sec. V. Some numerical results are shown in Fig. 6.

We use the following arclength parametrization of the tangent vector:

$$t^{\mu} = \begin{pmatrix} e^{A(\rho)}\sinh\zeta \\ e^{A(\rho)}\cos\delta\cosh\zeta \\ \sin\delta\cosh\zeta \end{pmatrix}, \tag{C5}$$

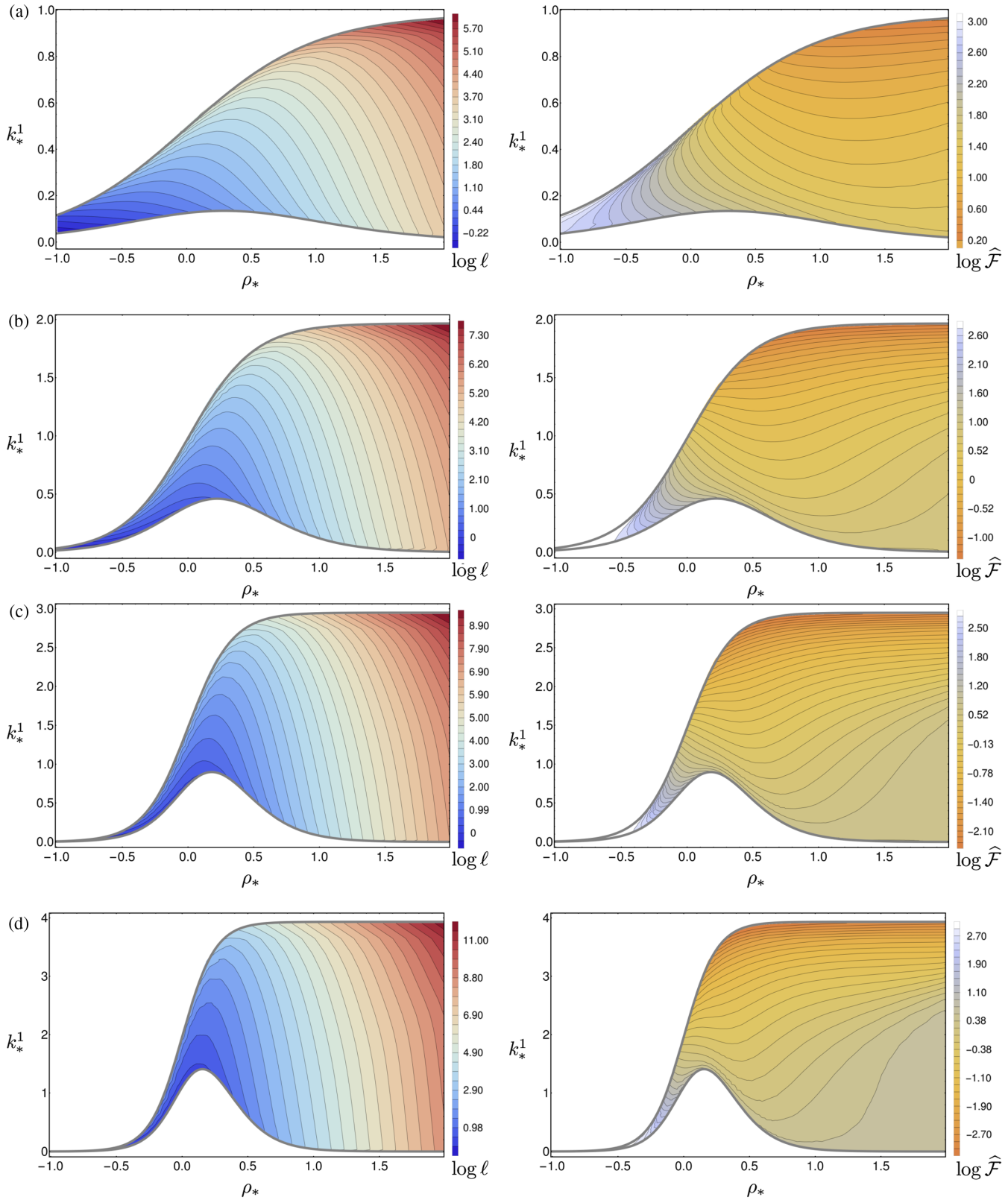

FIG. 6. As in Fig. 5, we show the contour plots of ℓ and $\hat{\mathcal{F}}$ within the escape regions at the chiral point, now for the domain wall metric (C2). From panels (a) to (d) we increase $L_{\mathrm{UV}}/L_{\mathrm{IR}}$ from 2 to 5. In all cases there is a critical contour: the only commonly valid prescription for the c-function is to choose asymptotically geodesic helices.

with orthogonal frame

$$n^{1\mu} = \begin{pmatrix} 0 \\ e^{A(\rho)}\sin\delta \\ -\cos\delta \end{pmatrix}, \quad n^{2\mu} = \begin{pmatrix} e^{A(\rho)}\cosh\zeta \\ e^{A(\rho)}\cos\delta\sinh\zeta \\ \sin\delta\sinh\zeta \end{pmatrix}. \tag{C6}$$

The associated curvatures and torsion are

$$\begin{aligned} k^1 &= A'(\rho)\cos\delta + \dot{\delta}\cosh\zeta, \\ k^2 &= \dot{\zeta} - A'(\rho)\sin\delta\sinh\zeta, \qquad \tau = -\dot{\delta}\sinh\zeta. \end{aligned} \tag{C7}$$

The shape equations are given by

$$\begin{aligned} &\mathfrak{m}(A'(\rho)\cos\delta + \dot{\delta}\cosh\zeta) \\ &\quad + \mathfrak{s}[\ddot{\zeta} + \cosh\zeta(\dot{\delta}^2\sinh\zeta - A'(\rho)\dot{\zeta}\sin\delta)] = 0, \end{aligned} \tag{C8}$$

$$\begin{aligned} &\mathfrak{m}(A'(\rho)\sin\delta\sinh\zeta - \dot{\zeta}) \\ &\quad + \mathfrak{s}[-\cosh\zeta\ddot{\delta} + \dot{\delta}(A'(\rho)\sin\delta\cosh^2\zeta - 2\dot{\zeta}\sinh\zeta)] = 0. \end{aligned} \tag{C9}$$

Not surprisingly, all of the above expressions can be obtained from their analogues of Sec. V by replacing $f(z)/L_{\mathrm{UV}} \to A'(\rho)$. By imposing the tip-defining condition $\dot{\rho}(0) = 0$, with fixed values for ρ_*, ζ_*, k^1_*, and k^2_*, we get

$$\delta_* = 0, \qquad \dot{\delta}_* = (k^1_* - A'(\rho_*))\mathrm{sech}\zeta_*, \qquad \dot{\zeta}_* = k^2_*. \tag{C10}$$

The Noether charges are given by

$$\mathcal{Q}_t = -e^{-A(\rho)}(\mathfrak{m}\sinh\zeta + \mathfrak{s}\dot{\delta}\cosh^2\zeta), \tag{C11}$$

$$\begin{aligned} \mathcal{Q}_x = e^{-A(\rho)}&[\mathfrak{m}\cos\delta\cosh\zeta \\ &+ \mathfrak{s}(\dot{\delta}\cos\delta\cosh\zeta\sinh\zeta - \dot{\zeta}\sin\delta)], \end{aligned} \tag{C12}$$

$$\mathcal{Q}_b = x\mathcal{Q}_t + t\mathcal{Q}_x + \sigma\cosh\zeta\sin\delta. \tag{C13}$$

Again, the tip condition imposes $\mathcal{Q}_b = 0$. The two remaining charges, evaluating the charges at the tip, can be written as

$$\begin{pmatrix} \mathcal{Q}_t \\ \mathcal{Q}_x \end{pmatrix} = e^{-A_*}\begin{pmatrix} \cosh\zeta_* & -\sinh\zeta_* \\ -\sinh\zeta_* & \cosh\zeta_* \end{pmatrix}\begin{pmatrix} \mathfrak{s}(A'_* - k^1_*) \\ \mathfrak{m} \end{pmatrix}. \tag{C14}$$

APPENDIX D: MATCHING CHARGES

In this section we connect the Mathisson helices behavior at the boundary with their tip values, eventually with the objective of proving Eq. (4.13). To this purpose, we exploit the fact that solutions to the shape equations (2.3) are asymptotically AdS_3 helices of the form (B1). Since each helix might have a different asymptotic behavior on either of its boundary end points, we will supply the notation of $(r, \eta, \Delta^t, \Delta^x)$ of Appendix B with a $(\pm)$ superscript to indicate whether they refer to the $s \to \pm\infty$ limits. The conserved charges $\mathcal{Q}_t$ and $\mathcal{Q}_x$ can be expressed in two different ways, using tip [see (5.10)] and boundary [see (B9)] quantities. By comparing these two expressions, we can solve for the dilatations $r^{(\pm)}$ and boost $\eta^{(\pm)}$ boundary parameters, finding

$$r^{(\pm)} = 2\mathfrak{s}z_*\sqrt{\frac{(\lambda^{(\pm)}_+)^2 - (\lambda^{(\pm)}_-)^2}{\mathfrak{s}^2\dot{\delta}^2_*\cosh(\zeta_*)^2 - \mathfrak{m}^2}}, \tag{D1}$$

$$\eta^{(\pm)} = -\zeta_* + \frac{1}{2}\log\left[\frac{(\mathfrak{s}\dot{\delta}_*\cosh\zeta_* - \mathfrak{m})(\lambda^{(\pm)}_+ - \lambda^{(\pm)}_-)}{(\mathfrak{s}\dot{\delta}_*\cosh\zeta_* + \mathfrak{m})(\lambda^{(\pm)}_+ + \lambda^{(\pm)}_-)}\right]. \tag{D2}$$

Since $\mathcal{Q}_b = 0$ we have that (B12) holds on both end points, i.e.,

$$\mathcal{Q}_x\Delta^{t(\pm)} + \mathcal{Q}_t\Delta^{x(\pm)} = 0. \tag{D3}$$

The significance of these relations relies on the fact that we can use them to find the length ℓ and the rapidity κ of the interval bounded by end points $(T_\pm, X_\pm)$. For helices isometric to $\gamma^\mu_{I_a}$ or $\gamma^\mu_{I_c}$, we find that

$$T_\pm = \Delta^{t(\pm)} \mp r^{(\pm)}\sinh(\eta^{(\pm)}), \tag{D4}$$

$$X_\pm = \Delta^{x(\pm)} \pm r^{(\pm)}\cosh(\eta^{(\pm)}). \tag{D5}$$

Using these relations and Eq. (4.4) we get

$$\Delta^{t(+)} - \Delta^{t(-)} = \ell\sinh\kappa + \frac{1}{2}(r^{(+)}\sinh\eta^{(+)} + r^{(-)}\sinh\eta^{(-)}), \tag{D6}$$

$$\Delta^{x(+)} - \Delta^{x(-)} = \ell\cosh\kappa - \frac{1}{2}(r^{(+)}\cosh\eta^{(+)} + r^{(-)}\cosh\eta^{(-)}). \tag{D7}$$

By substituting the relations (D6) and (D7) into (4.12) we find that

$$\left[\frac{\partial\gamma^\mu}{\partial\ell} - \frac{\dot{\gamma}^\mu}{\dot{z}}\frac{\partial z}{\partial\ell}\right]^{+s_\epsilon}_{-s_\epsilon} = \begin{pmatrix} \sinh\kappa \\ \cosh\kappa \\ 0 \end{pmatrix}, \tag{D8}$$

and therefore

$$\hat{\mathcal{F}}[\gamma(\ell)] = \ell(\mathcal{Q}_t[\gamma]\sinh\kappa + \mathcal{Q}_x[\gamma]\cosh\kappa). \tag{D9}$$

[1] A. B. Zamolodchikov, Irreversibility of the flux of the renormalization group in a 2D field theory, Pis'ma Zh. Eksp. Teor. Fiz. **43**, 565 (1986) [JETP Lett. **43**, 730 (1986)].
[2] F. Bastianelli and U. Lindstrom, C theorem for two-dimensional chiral theories, Phys. Lett. B **380**, 341 (1996).
[3] J. D. Brown and M. Henneaux, Central charges in the canonical realization of asymptotic symmetries: An example from three-dimensional gravity, Commun. Math. Phys. **104**, 207 (1986).
[4] S. Deser, R. Jackiw, and S. Templeton, Three-Dimensional Massive Gauge Theories, Phys. Rev. Lett. **48**, 975 (1982).
[5] K. Hotta, Y. Hyakutake, T. Kubota, and H. Tanida, Brown-Henneaux's canonical approach to topologically massive gravity, J. High Energy Phys. 07 (2008) 066.
[6] W. Li, W. Song, and A. Strominger, Chiral gravity in three dimensions, J. High Energy Phys. 04 (2008) 082.
[7] H. Casini and M. Huerta, A Finite entanglement entropy and the c-theorem, Phys. Lett. B **600**, 142 (2004).
[8] H. Liu and M. Mezei, A refinement of entanglement entropy and the number of degrees of freedom, J. High Energy Phys. 04 (2013) 162.
[9] S. Ryu and T. Takayanagi, Holographic Derivation of Entanglement Entropy from AdS/CFT, Phys. Rev. Lett. **96**, 181602 (2006).
[10] R. C. Myers and A. Singh, Comments on holographic entanglement entropy and RG flows, J. High Energy Phys. 04 (2012) 122.
[11] J. Camps, Generalized entropy and higher derivative gravity, J. High Energy Phys. 03 (2014) 070.
[12] X. Dong, Holographic entanglement entropy for general higher derivative gravity, J. High Energy Phys. 01 (2014) 044.
[13] P. Fonda, V. Jejjala, and A. Veliz-Osorio, On the shape of things: From holography to elastica, Ann. Phys. (Amsterdam) **385**, 358 (2017).
[14] A. Castro, S. Detournay, N. Iqbal, and E. Perlmutter, Holographic entanglement entropy and gravitational anomalies, J. High Energy Phys. 07 (2014) 114.
[15] P. Fonda, D. Liska, and l. Vliz-Osorio, Spinning probes and helices in AdS_3, Classical Quantum Gravity **35**, 185002 (2018).
[16] M. Mathisson, Neue mechanik materieller systemes, Acta Phys. Pol. **6**, 163 (1937).
[17] A. Papapetrou, Spinning test particles in general relativity. 1., Proc. R. Soc. A **209**, 248 (1951).
[18] W. G. Dixon, Dynamics of extended bodies in general relativity. II. Moments of the charge-current vector, Proc. R. Soc. A **319**, 509 (1970).
[19] M. Mathisson, Das zitternde Elektron und seine Dynamik, Acta Phys. Pol. **6**, 218 (1937).
[20] F. A. E. Pirani, On the physical significance of the Riemann tensor, Acta Phys. Pol. **15**, 389 (1956); Republication of: On the physical significance of the Riemann tensor, Gen. Relativ. Gravit. **41**, 1215 (2009).
[21] F. Costa, C. A. R. Herdeiro, J. Natario, and M. Zilhao, Mathisson's helical motions for a spinning particle: Are they unphysical?, Phys. Rev. D **85**, 024001 (2012).
[22] R. Hojman and S. Hojman, Spinning charged test particles in a Kerr-Newman background, Phys. Rev. D **15**, 2724 (1977).
[23] R. Capovilla and J. Guven, Geometry of deformations of relativistic membranes, Phys. Rev. D **51**, 6736 (1995).
[24] B. Carter, Essentials of classical brane dynamics, Int. J. Theor. Phys. **40**, 2099 (2001).
[25] M. Bañados and I. A. Reyes, A short review on Noethers theorems, gauge symmetries and boundary terms, Int. J. Mod. Phys. D **25**, 1630021 (2016).
[26] J. de Boer, E. P. Verlinde, and H. L. Verlinde, On the holographic renormalization group, J. High Energy Phys. 08 (2000) 003.
[27] M. Berg and H. Samtleben, An exact holographic RG flow between 2-d conformal fixed points, J. High Energy Phys. 05 (2002) 006.
[28] A. Belin, A. Castro, and L.-Y. Hung, Fake gaps in AdS_3/CFT_2, J. High Energy Phys. 11 (2015) 145.
[29] A. Bagchi, R. Basu, D. Grumiller, and M. Riegler, Entanglement Entropy in Galilean Conformal Field Theories and Flat Holography, Phys. Rev. Lett. **114**, 111602 (2015).
[30] S. M. Hosseini and A. Véliz-Osorio, Gravitational anomalies, entanglement entropy, and flat-space holography, Phys. Rev. D **93**, 046005 (2016).
[31] T. Azeyanagi, R. Loganayagam, and G. S. Ng, Anomalies, Chern-Simons terms and black hole entropy, J. High Energy Phys. 09 (2015) 121.
[32] T. Nishioka and A. Yarom, Anomalies and entanglement entropy, J. High Energy Phys. 03 (2016) 077.
[33] N. Iqbal and A. C. Wall, Anomalies of the entanglement entropy in Chiral theories, J. High Energy Phys. 10 (2016) 111.
[34] T. L. Hughes, R. G. Leigh, O. Parrikar, and S. T. Ramamurthy, Entanglement entropy and anomaly inflow, Phys. Rev. D **93**, 065059 (2016).